IEEE Access
Multidisciplinary ⋮ Rapid Review ⋮ Open Access Journal

Received March 15, 2022, accepted April 7, 2022, date of publication April 12, 2022, date of current version April 22, 2022.

Digital Object Identifier 10.1109/ACCESS.2022.3166810

Stability Assessment and Enhanced Control of DFIG-Based WTs During Weak AC Grid

ZHI LI, HAILIANG XU, (Member, IEEE), ZHONGXING WANG, AND QINGZENG YAN
College of New Energy, China University of Petroleum (East China), Qingdao 266580, China

Corresponding author: Hailiang Xu (xuhl@zju.edu.cn)

This work was supported in part by the National Natural Science Foundation of China under Grant 52077222, and in part by the Fundamental Research Funds for the Central Universities under Grant 19CX02016A.

ABSTRACT According to the latest grid codes, wind turbines (WTs) are required to inject certain amount of reactive and active current into the faulty grid during voltage sags. However, studies have shown that the doubly fed induction generator (DFIG)-based WTs may lose stability under weak grid condition. So the impact of grid code requirement on DFIG system stability is worthy of investigation. To address such issue, a comprehensive small-signal admittance model of DFIG system is established in this paper. Then the influence of reactive/active current settings during grid fault is analyzed in detail. Furthermore, the stable operation region is derived, considering three key factors, i.e., the current demand of grid codes, capacity of WTs and stability constraint. Besides, in order to extend the stable operation region of the DFIG system, an enhanced control strategy based on voltage disturbance compensation is put forward. Finally, simulations and experiments are performed to validate the correctness of the theoretical analysis and effectiveness of the proposed control.

INDEX TERMS Doubly fed induction generator (DFIG), impedance modelling, small-signal stability, enhanced control, disturbance compensation.

NOMENCLATURE

$\boldsymbol{U}$, $\boldsymbol{I}$, Ψ	Voltage, current and flux linkage vectors.
ω_s, ω_r	Synchronous and rotor angular frequency.
R_s, R_r	Stator and rotor resistances of DFIG.
L_s, L_r, L_m	Stator, rotor and mutual inductances of DFIG.
R_g, L_g	Resistance and inductance of grid-side reactor.
θ_{pll}, ω_{pll}	Output angle and angular frequency of PLL.
θ_{slip}, ω_{slip}	Slip angle and angular frequency
Subscripts	
s, r, g	Stator-, rotor- and grid-side quantities.
d, q	Dq-axis components.
Superscripts	
b, c	Grid- and PLL- reference frame.
$*$	Reference value.

The associate editor coordinating the review of this manuscript and approving it for publication was Zhixiang Zou.

I. INTRODUCTION

Due to the superiorities of low equipment cost, small converter capacity, wide operating range, and high reliability, the doubly fed induction generator (DFIG)-based wind turbines (WTs) have been the mainstream type of wind power generations [1], [2]. At the same time, grid codes have put forward strict requirement for grid-connected WTs, such as the well-known low voltage ride-through (LVRT), which not only prohibits WTs to be disconnected when the grid voltage is above the given profile, but also demand WTs to inject reactive/active current to restore the gird voltage [3]. As with the DFIG-based WTs, since the stator windings are directly tied into weak power grid, the DFIG system is fairly sensitive to grid disturbances, especially to grid dip fault [4].

However, due to the reverse distribution between wind power resources and power loads, large-scale wind farms are usually integrated into power grid through long-distance transmission lines [5]. If the short-circuit ratio (SCR) is less than 3, the grid is usually regarded as a weak grid [6]. When the fault occurs in weak AC grid, the high impedance of long-distance transmission line may be the key factor that leads to the failure of conventional LVRT control strategy [5],

This work is licensed under a Creative Commons Attribution 4.0 License. For more information, see https://creativecommons.org/licenses/by/4.0/

and even leads to instability if the system control coefficients are not set properly [7]. Hence, the stability issue of DFIG-based WTs connected into weak grid has attracted more and more attention [3], [5]–[18].

In [3], [8], based on the power angle and small interference stability theory of synchronous machine, the state space model of DFIG-based WTs is set up, where the influence of phase-locked loop (PLL) parameters on system stability is analyzed. A small-signal model of DFIG, including its rotor-side converter (RSC), is established in [9], where the stability influence of control parameters of RSC is discussed. Similar model is presented in [10], and modal analysis shows that the system stability is mainly affected by the PLL, rotor current controller (RCC), and the terminal voltage as well. It is noteworthy that the above stability studies mainly focus on normal grid conditions.

In [11]–[14], the instability mechanism of DFIG system during weak grid fault is explored. It is found that the controller bandwidth under normal grid condition is no longer applicable to that of the fault condition, due to the complex interaction between the controller and weak AC grid. And some improved LVRT schemes have been proposed during symmetrical grid faults [11], [13].

As for stability analysis, the state space methods are usually adopted. However, the calculation burden, caused by the high order equations, makes it unacceptable when the methods are applied to complicated systems [15]. In the contrast, the impedance-based methods are widely used, since the calculation burden is moderate, while the physical meanings is clear. In [15], the impedance model of the RSC is established and the interaction between the DFIG-based WTs and weak power grid is studied. In [16], [17], a unified impedance model of DFIG-based WTs including the grid-side converter (GSC) is further proposed, and the transmission relationship from the grid voltage disturbance to the controller output is then analyzed. However, in regard to the current supporting requirement by the grid codes, the influence of reactive and active current injection on system stability still remains unknown.

To address such issue, this paper firstly establishes a small-signal admittance model of DFIG-based WTs tied into weak AC grids, considering the effects of PLL, RCC, and line impedance as well. Then the influence of reactive/active current settings during grid dips is analyzed in detail. Furthermore, the stable operation range is derived, considering three key factors, i.e., the current demand of grid codes, capacity of WTs and stability restriction. In order to improve the stability of DFIG during weak grid fault, an enhanced control strategy based on voltage disturbance compensation is put forward. Finally, simulations and experiments are carried out to validate the correctness of the analysis and effectiveness of the proposed control.

II. SMALL-SIGNAL MODELING OF THE DFIG SYSTEM

In order to analyze the stability of the DFIG system, a small-signal admittance model of DFIG in the synchronous reference frame (SRF) is firstly established. The structure diagram and control loops of the DFIG tied into weak AC grid is given in Fig. 1.

The existing research shows that the stability of DFIG is mainly determined by RSC, while the influence of GSC is very limited [11], [15]. Therefore, this paper focuses on the modelling and stability analysis of the RSC. The small-signal model is composed of the main circuit of DFIG, the RSC and the corresponding control system. The modelling process are given in the following.

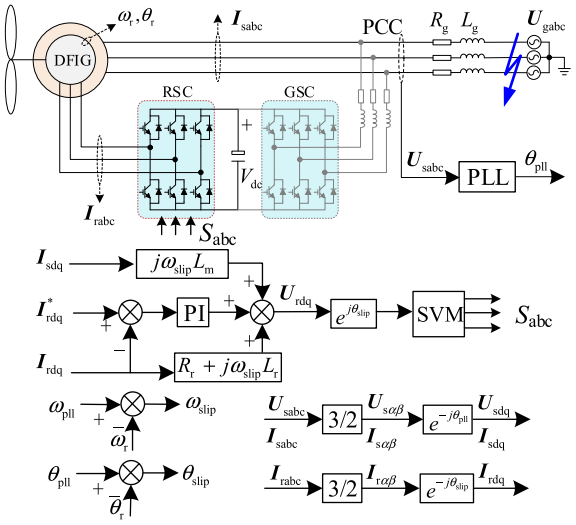

FIGURE 1. Diagram and control loops of DFIG tied into weak AC grid.

A. DFIG MODEL

According to the voltage and flux equation of DFIG in the SRF system, the expression of the stator and rotor voltage for the rotor current can be obtained as:

$$\hat{\boldsymbol{I}}_{\mathrm{rdq}} = \boldsymbol{G}_{\mathrm{sr}}\hat{\boldsymbol{U}}_{\mathrm{sdq}} + \boldsymbol{G}_{\mathrm{rr}}\hat{\boldsymbol{U}}_{\mathrm{rdq}} \tag{1}$$

$$\begin{cases} \boldsymbol{G}_{\mathrm{rr}} = \dfrac{1}{a^2+b^2}\begin{bmatrix} a & b \\ -b & a \end{bmatrix} \\ \boldsymbol{G}_{\mathrm{sr}} = \dfrac{1}{a^2+b^2}\begin{bmatrix} bd-ac & -(ad+bc) \\ ad+bc & bd-ac \end{bmatrix} \end{cases} \tag{2}$$

where

$$\begin{cases} a = K_1 L_{\mathrm{m}}\left(\omega_{\mathrm{slip}}\omega_{\mathrm{s}}L_{\mathrm{m}}R_{\mathrm{s}} - sK_2\right) + (R_r + sL_{\mathrm{r}}) \\ b = -K_1 L_{\mathrm{m}}\left(s\omega_{\mathrm{s}}L_{\mathrm{m}}R_{\mathrm{s}} + \omega_{\mathrm{slip}}K_2\right) + \omega_{\mathrm{slip}}L_{\mathrm{r}} \\ c = sK_1 L_{\mathrm{m}}\left(R_{\mathrm{s}} + sL_{\mathrm{s}}\right) + K_1 L_{\mathrm{m}}\omega_{\mathrm{slip}}\omega_{\mathrm{s}}L_{\mathrm{s}} \\ d = -K_1 L_{\mathrm{m}}\omega_{\mathrm{slip}}\left(R_{\mathrm{s}} + sL_s\right) + sK_1 L_{\mathrm{m}}\omega_{\mathrm{s}}L_{\mathrm{s}}, \end{cases}$$

and $\begin{cases} K_1 = 1/\left[(R_{\mathrm{s}} + sL_{\mathrm{s}})^2 + \omega_{\mathrm{s}}^2 L_{\mathrm{s}}^2\right] \\ K_2 = sL_{\mathrm{m}}\left(R_{\mathrm{s}} + sL_{\mathrm{s}}\right) + \omega_{\mathrm{s}}^2 L_{\mathrm{s}}L_{\mathrm{m}} \end{cases}$.

Similarly, the expression of stator voltage and rotor current for stator current can be obtained as:

$$\hat{\boldsymbol{I}}_{\mathrm{sdq}} = \boldsymbol{G}_{\mathrm{ss}}\hat{\boldsymbol{U}}_{\mathrm{sdq}} + \boldsymbol{G}_{\mathrm{rs}}\hat{\boldsymbol{I}}_{\mathrm{rdq}} \tag{3}$$

$$\begin{cases} \boldsymbol{G}_{\rm ss} = K_1 \begin{bmatrix} R_{\rm s} + sL_{\rm s} & \omega_{\rm s}L_{\rm s} \\ -\omega_{\rm s}L_{\rm s} & R_{\rm s} + sL_{\rm s} \end{bmatrix} \\ \boldsymbol{G}_{\rm rs} = K_1 \begin{bmatrix} -K_2 & \omega_{\rm s}L_{\rm m}R_{\rm s} \\ -\omega_{\rm s}L_{\rm m}R_{\rm s} & -K_2 \end{bmatrix} \end{cases} \tag{4}$$

Accordingly, the small-signal model of the DFIG main circuit can be described as Fig. 2.

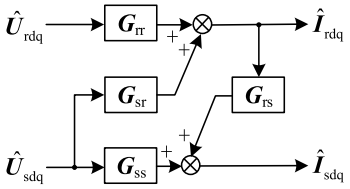

FIGURE 2. The small-signal model of the DFIG main circuit.

B. PLL MODEL

As shown in Fig. 3, when the grid voltage is disturbed, the phase information of the power grid obtained through the PLL, will deviate from that of the actual one, which will further lead to disturbance in the control system. In order to estimate the influence of such disturbance, two SRFs are introduced, i.e., the grid dq frame represented by superscript 'b', and the PLL dq frame represented by superscript 'c'.

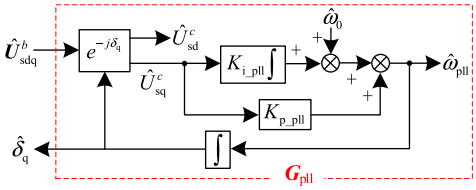

FIGURE 3. Structure diagram of the PLL.

According to Fig. 3, the small signal dynamic characteristics of the PLL can be expressed as:

$$\hat{\boldsymbol{\delta}}_{\rm dq} = \boldsymbol{G}_{\rm pll}\hat{\boldsymbol{U}}^b_{\rm sdq} \tag{5}$$

where $\boldsymbol{G}_{\rm pll} = \begin{bmatrix} 0 & 0 \\ 0 & H_{\rm pll} \end{bmatrix}$, and $H_{\rm pll} = \frac{(sK_{\rm p\_pll}+K_{\rm i\_pll})}{s^2+U^b_{\rm sd0}(sK_{\rm p\_pll}+K_{\rm i\_pll})}$;

with $K_{\rm p\_pll}$ and $K_{\rm i\_pll}$ being the proportional and integration coefficients of the PI controllers of PLL.

By linearization, the relationship between the stator current in the grid dq^b frame and PLL dq^c frame can be expressed as:

$$\hat{\boldsymbol{I}}^c_{\rm sdq} = \hat{\boldsymbol{I}}^b_{\rm sdq} + \boldsymbol{G}_{\rm is}\hat{\boldsymbol{\delta}}_{\rm dq} \tag{6}$$

where $\boldsymbol{G}_{\rm is} = \begin{bmatrix} 0 & I^b_{\rm sd} \\ 0 & -I^b_{\rm sd} \end{bmatrix}$.

Similarly, We Can Obtain

$$\boldsymbol{G}_{\rm ir} = \begin{bmatrix} 0 & I^b_{\rm rq} \\ 0 & -I^b_{\rm rq} \end{bmatrix}, \boldsymbol{G}_{\rm ur} = \begin{bmatrix} 0 & U^b_{\rm rd} \\ 0 & -U^b_{\rm rd} \end{bmatrix}, \boldsymbol{G}_{\rm us} = \begin{bmatrix} 0 & U^b_{\rm sd} \\ 0 & -U^b_{\rm sd} \end{bmatrix}.$$

C. RSC CURRENT CONTROL LOOP MODEL

The proportional-integral (PI) controller is commonly used in the rotor current loop, and the small-signal model of the rotor voltage in the PLL dq^c fame can then be expressed as:

$$\begin{bmatrix} \hat{U}^c_{\rm rd} \\ \hat{U}^c_{\rm rq} \end{bmatrix} = (\boldsymbol{G}_{\rm d1} - \boldsymbol{G}_{\rm rcc}) \begin{bmatrix} \hat{I}^c_{\rm rd} \\ \hat{I}^c_{\rm rq} \end{bmatrix} + \boldsymbol{G}_{\rm d2} \begin{bmatrix} \hat{I}^c_{\rm sd} \\ \hat{I}^c_{\rm sq} \end{bmatrix} \tag{7}$$

where

$$\boldsymbol{G}_{\rm rcc} = \begin{bmatrix} K_{\rm p\_rcc} + K_{\rm i\_rcc}/s & 0 \\ 0 & K_{\rm p\_rcc} + K_{\rm i\_rcc}/s \end{bmatrix},$$
$$\boldsymbol{G}_{\rm d1} = \begin{bmatrix} R_{\rm r} & -\omega_{\rm slip}L_{\rm r} \\ \omega_{\rm slip}L_{\rm r} & R_{\rm r} \end{bmatrix}, \boldsymbol{G}_{\rm d2} = \begin{bmatrix} 0 & -\omega_{\rm slip}L_{\rm m} \\ \omega_{\rm slip}L_{\rm m} & 0 \end{bmatrix};$$

$K_{\rm p\_rcc}$ and $K_{\rm i\_rcc}$ being the proportional and integration coefficients of the PI controller in the RSC.

D. INTEGRATED SYSTEM MODEL

Based on the previous derivation, the DFIG small-signal model including both the RSC current control and PLL can be obtained, as shown in Fig. 4.

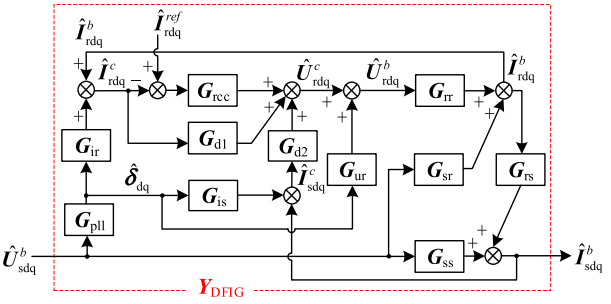

FIGURE 4. The small-signal model of DFIG including RSC current control and PLL.

Note that, in the small-signal stability analysis, the rotor current reference can be regarded as a constant, thus its small disturbance $\hat{\boldsymbol{I}}^{ref}_{\rm rdq}$ is equal to zero.

According to (1)-(7) and Fig. 4, the small-signal dynamic characteristics of DFIG including RSC current control and PLL can be expressed as:

$$\hat{\boldsymbol{I}}^b_{\rm sdq} = \mathbf{Y}_{\rm DFIG}\hat{\boldsymbol{U}}^b_{\rm sdq} \tag{8}$$

where $\begin{cases} \mathbf{Y}_{\rm DFIG} = (\mathbf{E} - \boldsymbol{G}_{\rm d2}\boldsymbol{G}_{\rm rs}\boldsymbol{G}_3)^{-1}\boldsymbol{G}_4 \\ \boldsymbol{G}_1 = \boldsymbol{G}_{\rm d1} - \boldsymbol{G}_{\rm rcc} \\ \boldsymbol{G}_2 = \boldsymbol{G}_1\boldsymbol{G}_{\rm ir}\boldsymbol{G}_{\rm pll} + \boldsymbol{G}_{\rm d2}\boldsymbol{G}_{\rm is}\boldsymbol{G}_{\rm pll} - \boldsymbol{G}_{\rm ur}\boldsymbol{G}_{\rm pll} \\ \boldsymbol{G}_3 = (\mathbf{E} - \boldsymbol{G}_{\rm rr}\boldsymbol{G}_1)^{-1} \\ \boldsymbol{G}_4 = \boldsymbol{G}_{\rm rs}\boldsymbol{G}_3\,(\boldsymbol{G}_{\rm sr}\boldsymbol{G}_1 + \boldsymbol{G}_2) + \boldsymbol{G}_{\rm ss} \end{cases}$, and $\boldsymbol{E}$ represent the identify matrix.

The improved model comprehensively considers the DFIG, current loop control, phase-locked loop and frame rotating transformation. In particular, the model takes into account the coupling between the d- and q-axis in vector control and the frame rotating inverse transformation of the rotor voltage, as shown in Fig. 4.

Due to the existence of asymmetrical factors, such as PLL, the d- and q-axis of the DFIG system are asymmetrical, which

results in the transfer function from the voltage to current being a 2 × 2 admittance matrix, i.e.,

$$\boldsymbol{Y}_{\mathrm{DFIG}} = \begin{bmatrix} Y_{\mathrm{dd}} & Y_{\mathrm{qd}} \\ Y_{\mathrm{dq}} & Y_{\mathrm{qq}} \end{bmatrix} \tag{9}$$

Fig. 5 shows the calculated Bode diagrams of the DFIG input admittance ($\boldsymbol{Y}_{\mathrm{DFIG}}$), compared to those obtained using frequency sweep method in a time-domain simulation model [15], [16]. As seen, the results match well, which validates the correctness of the proposed model.

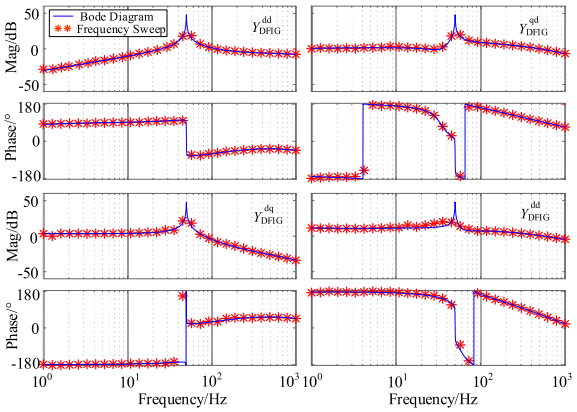

FIGURE 5. Frequency sweep results of DFIG-based WT.

III. STABILITY ANALYSIS AND VOLTAGE DISTURBANCE COMPENSATION CONTROL STRATEGY

According to the generalized Nyquist stability criterion, the stability of MIMO system is determined by the times that the Nyquist curve of the return-ratio matrix circles the point (−1, 0) counterclockwise. For the DFIG system, the return-ratio matrix is $\boldsymbol{L}(s) = \boldsymbol{Z}_{\mathrm{g}}(s)\boldsymbol{Y}_{\mathrm{DFIG}}(s)$, where $\boldsymbol{Y}_{\mathrm{DFIG}}(s)$ is the input admittance matrix of DFIG and $\boldsymbol{Z}_{\mathrm{g}}(s)$ is the grid impedance matrix, which can be described by

$$\boldsymbol{Z}_{\mathrm{g}} = \begin{bmatrix} R_{\mathrm{g}} + sL_{\mathrm{g}} & -\omega_{\mathrm{g}}L_{\mathrm{g}} \\ \omega_{\mathrm{g}}L_{\mathrm{g}} & R_{\mathrm{g}} + sL_{\mathrm{g}} \end{bmatrix} \tag{10}$$

On the basis of the obtained small-signal model, i.e., (8), the influence of the active and reactive current on stability during grid voltage dips can be analyzed. In this paper, the reactive and active current response requirements of the grid code in China (GB/T 19963-2011) is taken as an example.

A. INFLUENCE OF ACTIVE AND REACTIVE CURRENT ON STABILITY

In order to estimate the influence of the active current injected into the weak grid during grid voltage dips, assume that the voltage amplitude remain unchanged during the fault duration stage. For instance, when the grid voltage drops to 0.58p.u., the generalized Nyquist curves of the DFIG system with different active current can be drawn as Fig. 6.

As shown in Fig. 6, when the active current is set to be −0.3 p.u. (a), the Nyquist curve does not surround the point (−1, 0), which means that the system is stable at this time. However, when the active current is increased to −0.4p.u. (b), the Nyquist curve approaches the point (−1, 0), which indicates that increasing the active current is not conducive to system stability. In Fig. 6(c), the Nyquist curve gets to surround the point (−1, 0), when the active current is increased to -0.5p.u., implying that the system becomes unstable.

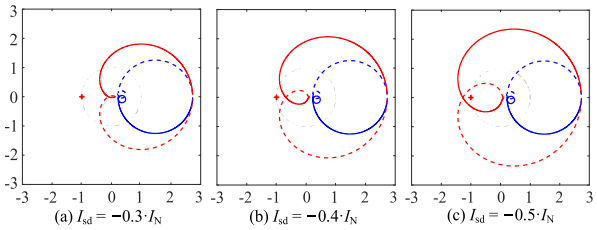

FIGURE 6. Generalized Nyquist curves varying with active current references.

Similarly, the impact of the reactive current on the stability can be studied based on the small-signal admittance model. The generalized Nyquist curves of the DFIG system with different reactive currents are shown in Fig. 7. It is notable that when the DFIG reactive current varies, the generalized Nyquist curve almost remained unchanged. It thus can be concluded that the reactive current has little influence on the stability of DFIG system.

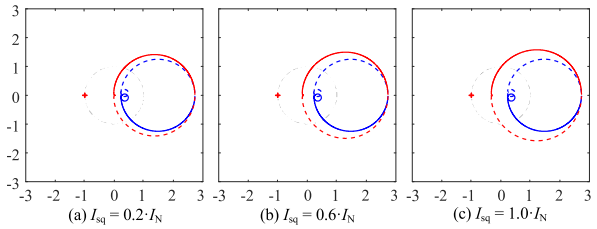

FIGURE 7. Generalized Nyquist curves varying with reactive current references.

In summary, it can be concluded that increasing the active current into the weak AC grid during voltage dips is not conducive to system stability and even leading to instability issue. However, changing the reactive current injected into the weak grid has little impact on the stability.

The reason lies in the interaction between the weak AC grid and DFIG turbine. As shown in Fig. 8, due to the considerable grid impedance, i.e., $R_{\mathrm{g}} + j\omega_{\mathrm{s}}L_{\mathrm{g}}$, the stator voltage will be distorted when a harmonic or resonant current is injected into the weak grid. Usually, the grid reactance is much larger than its resistance. Therefore, according to the formula surrounded by red box in Fig. 8, the active current I_{sd} will mainly affect the q-axis stator voltage, i.e., U_{sq}, while the reactive I_{sq} current will primarily impacts the d-axis stator voltage, i.e., U_{sd}. However, as depicted in the figure, only the disturbance in U_{sq} will be further transmitted to the DFIG control system through the PLL and rotating frame transformation process. Consequently, the influence of the active current is more remarkable than that of the reactive one.

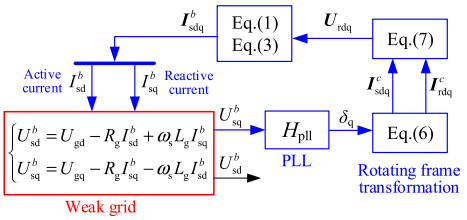

FIGURE 8. Interaction relationship between the weak grid and DFIG system.

B. COMPREHENSIVE CONSTRAINT OF THE ACTIVE AND REACTIVE CURRENT DURING GRID VOLTAGE DIPS

In addition to the stability constraint, two other restrictions need to be considered when setting the active and reactive currents, i.e., the grid code requirement and the capacity limit of DFIG turbine. Here, the grid code of China (GB/T 19963-2011) [16] is chosen as an example, with its essential requirement listed briefly as follows.

When the PCC voltage is within 20% to 90% of its nominal value, the WTs should be able to keep grid-connected and inject a certain amount of reactive current, which should be no less than

$$I_{\mathrm{q}} \geq 1.5 \times (0.9 - U_{\mathrm{t}})\, I_{\mathrm{N}},\ (0.2 \leq U_{\mathrm{t}} \leq 0.9) \tag{11}$$

where I_{q}denotes the required reactive current value according to the grid code; U_{t} represents the remaining voltage at the PCC.

For instance, when the voltage at PCC drops to 0.58 p.u., according to (11), the wind turbines should output reactive current (I_{sq}) to be no less than 0.48 p.u. Assume that the maximum current capacity of DFIG is within 1.2 p.u. Then, the DFIG stable operating region under such grid dips can be drawn, as the shadow region shown in Fig. 9, which is determined by three factors, i.e., the stability curve based on the small-signal model, the capacity limit of DFIG and the reactive current requirement by the grid code. If the voltage dip changes, it will directly affect the critical curve of the stability and the lower limit of reactive current in Fig. 9. As a result, it will affect the stable operating region. For example, if the voltage drops more, more reactive current is required, and the stable operating region will get shrink, as shown by the red arrow in Fig. 9.

It needs to be pointed out that the stability curve, marked in pink in Fig. 9, can be obtained according the stability analysis based on the generalized Nyquist stability criterion. It can be seen from Fig. 9 that although the DFIG is required to generate reactive current in priority during weak grid voltage dip, it still has some capacity to output active power. However, the active power is strictly restricted by the stability constraint. Hence, in order to improve the active power output capacity of the DFIG, a better way is to enhance the system stability under such adverse grid condition. In other words, an enhanced control is needed to increase the output capacity of the DFIG system.

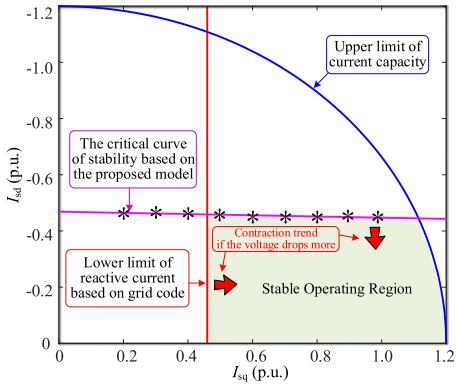

FIGURE 9. Comprehensive constraint of the active and reactive current during grid voltage dips.

C. ENHANCED CONTROL STRATEGY BASED ON VOLTAGE DISTURBANCE COMPENSATION

From the above analysis, it is obvious that the disturbance in the stator voltage will be transmitted into the whole control system through the PLL and frame rotating transformation, which will then influence the stability of the DFIG system. To reduce the impact of such disturbance, an enhanced control strategy based on voltage disturbance compensation is proposed. This control strategy is realized by compensating the disturbance in the rotor voltage, i.e., $\hat{\boldsymbol{U}}^{c}_{rdq}$, which corresponds to the grid voltage disturbance $\hat{\boldsymbol{U}}^{b}_{sdq}$ introduced through the PLL and rotating frame transformation process.

The proposed control structure is given in Fig. 10, where $\boldsymbol{G}_{\mathrm{filter}} = \begin{bmatrix} H_{\mathrm{fil}} & 0 \\ 0 & H_{\mathrm{fil}} \end{bmatrix}$, with H_{fil} being the transfer function of the second-order high pass filter, which is used to obtain the stator voltage disturbance. According to Fig. 10, the transfer function from the disturbance of the stator voltage to the output of the RSC can be obtained as

$$\boldsymbol{G}_{\mathrm{vsr}} = (\boldsymbol{G}_{\mathrm{d1}} - \boldsymbol{G}_{\mathrm{rcc}})\, \boldsymbol{G}_{\mathrm{ir}} \boldsymbol{G}_{\mathrm{pll}} + \boldsymbol{G}_{\mathrm{d2}} \boldsymbol{G}_{\mathrm{is}} \boldsymbol{G}_{\mathrm{pll}} - \boldsymbol{G}_{\mathrm{ur}} \boldsymbol{G}_{\mathrm{pll}} \tag{12}$$

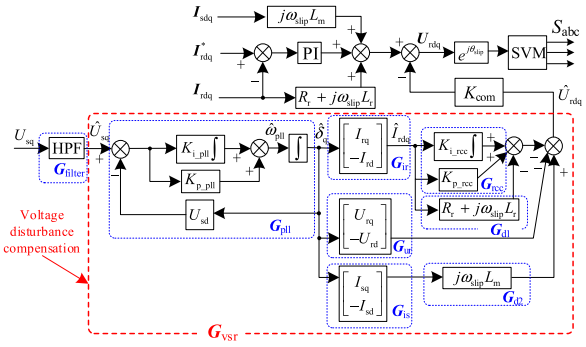

FIGURE 10. Control strategy based on voltage disturbance compensation.

In the design, a high-pass filter is firstly implemented to filter out the steady-state DC components of the stator voltage, and then the disturbance can be obtained. The disturbance transfer function, i.e., $\boldsymbol{G}_{\mathrm{com}}$, is further compensated

to the output of the rotor current loop, so as to enhance the system stability, $\boldsymbol{G}_{\text{com}} = K_{\text{com}}\boldsymbol{G}_{\text{vsr}}$, with K_{com} being the compensation coefficient.

Note that once the voltage disturbance compensation is applied, the admittance model of the DFIG system needs to be modified. The proposed control is equivalent to paralleling an auxiliary admittance with the original one, as shown in Fig.11. Then, the modified admittance of whole DFIG with voltage disturbance compensation can be obtained as

$$\boldsymbol{Y}'_{\text{DFIG}} = \boldsymbol{Y}_{\text{DFIG}} - \underbrace{\boldsymbol{G}_{\text{rs}}\boldsymbol{G}_5\left[\mathbf{E} - \boldsymbol{G}_{\text{d2}}\boldsymbol{G}_{\text{rs}}\boldsymbol{G}_5\right]^{-1}\boldsymbol{G}_{\text{com}}\boldsymbol{G}_{\text{filter}}\boldsymbol{G}_{\text{us}}\boldsymbol{G}_{\text{pll}}}_{\boldsymbol{Y}_{\text{com}}} \tag{13}$$

where $\boldsymbol{G}_5 = \boldsymbol{G}_{\text{rr}}\left[\mathbf{E} - (\boldsymbol{G}_{\text{d1}} - \boldsymbol{G}_{\text{rcc}})\,\boldsymbol{G}_{\text{rr}}\right]^{-1}$.

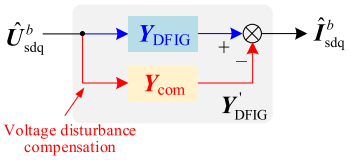

FIGURE 11. The small-signal model with voltage disturbance compensation.

To further investigate the influence of the proposed control, the generalized Nyquist curves are drawn before and after the control being triggered, as displayed in Fig. 12. It can be seen that the generalized Nyquist curve surrounds the point $(-1, 0)$ when the conventional control is used, which means that the system is unstable. Contrastively, once the voltage disturbance compensation works, the generalized Nyquist curve does not surround the point $(-1, 0)$, indicating that the system gets stable. Hence, the proposed control can effectively improve the stability of DFIG system during weak grid condition.

In addition, the proposed control strategy is compared with the virtual inductance control strategy. As shown in the Fig.12, the Nyquist curve of the proposed control strategy is farther away from the point $(-1,0)$, which indicates that the proposed control strategy has more stability margin than the virtual inductance control strategy.

As a result, the stable operation region of DFIG under grid dips can be redrawn, as shown in Fig. 13. Obviously, the stable operating region gets extended, compared with that in Fig. 9.

IV. SIMULATION AND EXPERIMENTAL VALIDATIONS

A. 5.5kW DFIG SIMULATION STUDIES

To validate the correctness of the stability analysis and the effectiveness of the proposed control, simulations were carried out with a 5.5kW DFIG under MATLAB/Simulink environment.

Firstly, the influence of outputted DFIG active current is studied. Fig. 14 shows the simulation waveforms of the DFIG turbine during the grid voltage at 0.58p.u. The active current

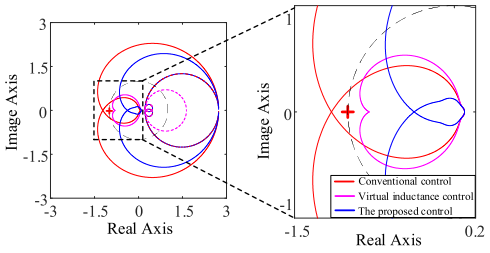

FIGURE 12. Generalized Nyquist curves of DFIG with different control strategies.

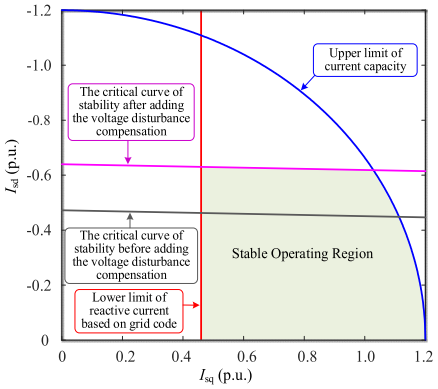

FIGURE 13. Comprehensive constraint of the active and reactive current during grid voltage dips.

is initially set as -0.3p.u., while at 0.6s, it increases to -0.4p.u. Note that the system remains stable during such process. However, at 0.8s, when the active current increases up to -0.5p.u., obvious oscillations gets to occur in the stator voltage and current, implying that the system loses its stability. This is consistent well with the stability analysis results in Fig. 6.

Similarly, the influence of DFIG reactive current on system stability is investigated. Fig. 15 shows the simulation results when the reactive current changes. Initially, the reactive current is set to be 0.2p.u., while at 0.6s it increases up to 0.6p.u. As can be seen, the stator voltage/current does not oscillate, and the system keeps stable. At 0.8s, when the reactive current reaches to 1.0, the DFIG system can still be stable, which is identical with the stability analysis in Fig. 7. An interesting phenomenon is that, after 0.8s, the disturbance in stator voltage mainly behaves in the d-axis component. Referring to the analysis in Chapter II-A, the disturbance of d-axis component will not be further transmitted to the control system of rotor side converter, so system remains stable. Hence, Fig. 15 proves the correctness of the stability analysis.

Finally, a test is performed to verify the effectiveness of the proposed control strategy. The time domain simulation results are exhibited in Fig. 16. At 0.8s, the active current injected into the weak grid increases from -0.4p.u. to -0.5p.u., oscillations get to occur in the stator voltage and current, and the system loses its stability. However, when the compensated control strategy is triggered at 1.1s., the oscillations are sup-

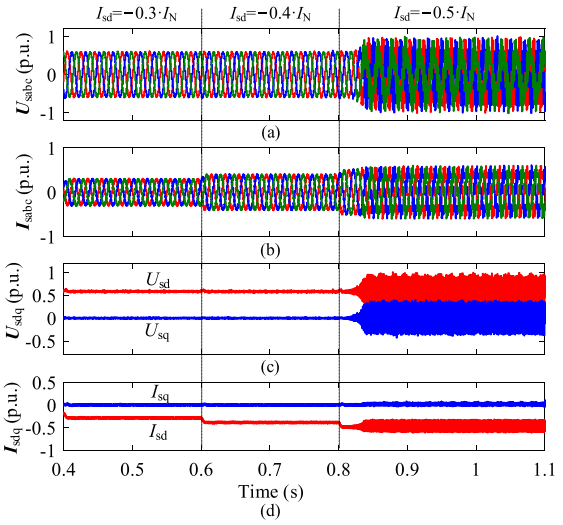

FIGURE 14. Time domain simulation waveforms when active current changes. (a) stator three-phase voltage U_{sabc}; (b) stator three-phase current I_{sabc}; (c) stator dq-axis voltage U_{sdq}; (d) stator dq-axis current I_{sdq}.

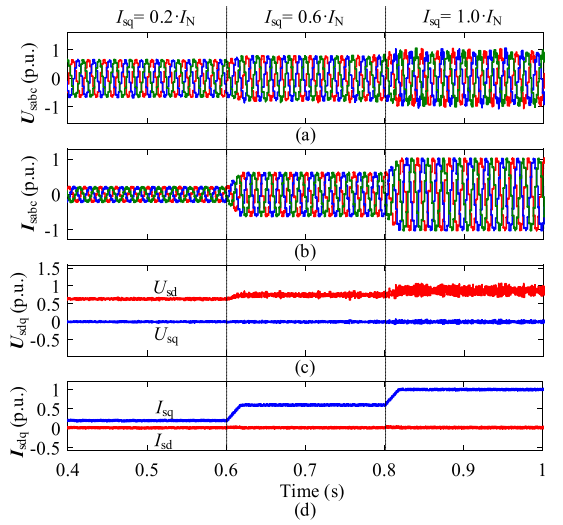

FIGURE 15. Time domain simulation waveforms when reactive current changes. (a) stator three-phase voltage U_{sabc}; (b) stator three-phase current I_{sabc}; (c) stator dq-axis voltage U_{sdq}; (d) stator dq-axis current I_{sdq}.

pressed significantly, and the DFIG system returns to a stable state. The simulation is consistent with the analysis result in Fig. 12.

B. 3.0MW DFIG SIMULATION STUDIES

In order to further verify the correctness of the stability analysis and the effectiveness of the proposed control, simulations were carried out with a 3.0MW DFIG as well, whose key parameters are given in Tab. 2.

The influence of reactive current on stability is shown in Fig. 17. The DFIG system is always stable when the reactive current increases from 0.2p.u. to 1.0p.u.. The influence of

TABLE 1. Parameters of the 3.0MW DFIG.

Rated power (MW)	3.0
Rated voltage (V)	690
Pole pairs	3
Turn ratio	2.857
Vdc (V)	1200
R_s (p.u.)	0.013
R_r (p.u.)	0.024
L_s (p.u.)	4.226
L_r (p.u.)	4.203
L_m (p.u.)	3.99
ω_r (r/min)	860
Fault voltage (p.u.)	0.6

TABLE 2. Parameters of the 5.5kW DFIG experimental platform.

Rated power (kW)	5.5
Rated voltage (V)	380
Pole pairs	3
Turn ratio	1.63
Vdc (V)	600
R_s (Ω)	1.1
R_r (Ω)	2.3
L_s (H)	0.129
L_r (H)	0.129
L_m (H)	0.123
ω_r (r/min)	800
Fault voltage (p.u.)	0.58

active current on stability and the effect of the proposed control strategy are shown in Fig. 18. When the active current increases from -0.4p.u to -0.5p.u at 0.8s, obvious oscillations gets to occur in the stator voltage and current, implying that the system loses its stability; At 1.1s, the control strategy proposed in this paper is adopted, then the DFIG system returns to a stable state. These simulation results are consistent with those carried out with a 5.5kW DFIG. This further verifies the correctness of the stability analysis and the effectiveness of the proposed control

C. EXPERIMENTAL VALIDATIONS

In order to further demonstrate the effectiveness and feasibility of the proposed control strategy during weak grid dips, a 5.5kW DFIG experimental platform based on DSP28335 is built, with its structure shown in Fig. 19. The key parameters of the experimental system are given in Tab. 2. The DFIG system is driven by a 3-phase induction motor, and the line impedance of the weak grid is simulated by connecting reactors in series with the power grid. The symmetrical grid fault is generated by the three-phase transformer. In addition,

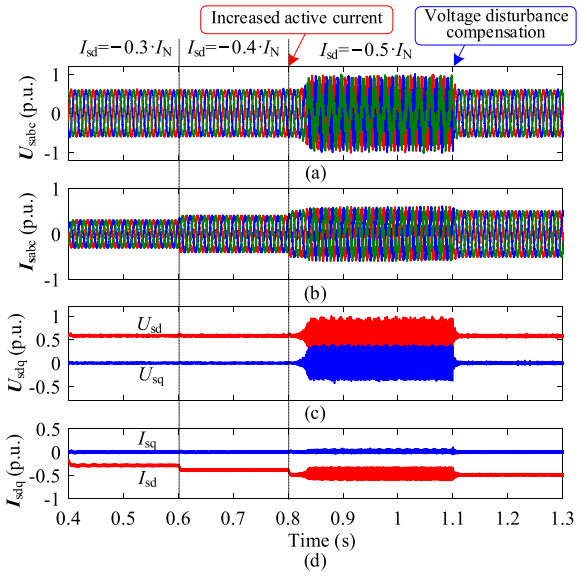

FIGURE 16. Time domain simulation results of DFIG with the proposed control strategy based on voltage disturbance compensation. (a) stator three-phase voltage U_{sabc}; (b) stator three-phase current I_{sabc}; (c) stator dq-axis voltage U_{sdq}; (d) stator dq-axis current I_{sdq}.

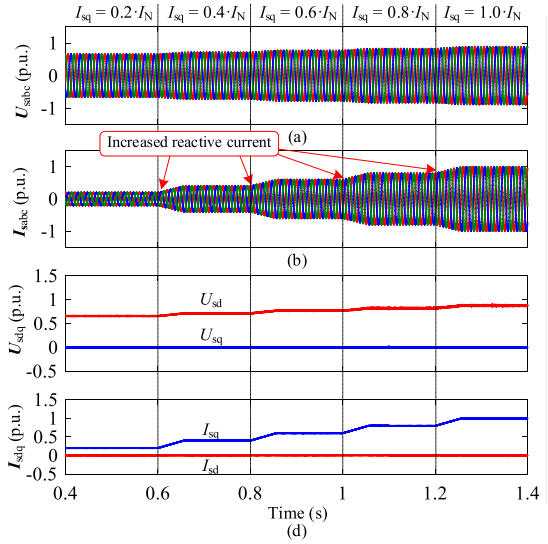

FIGURE 17. Time domain simulation waveforms when reactive current changes. (a) stator three-phase voltage U_{sabc}; (b) stator three-phase current I_{sabc}; (c) stator dq-axis voltage U_{sdq}; (d) stator dq-axis current I_{sdq}

a four-channel oscilloscope and host PC are used to observe and record the experimental waveforms. Meanwhile, the host PC is also used to send commands to the controller.

Fig. 20 presents the experimental waveforms of the DFIG turbine under the conventional and the proposed control, respectively, where the active current injected into the fault weak grid is set to be -0.4p.u. As shown in Fig. 20(A), when the DFIG is controlled by the conventional control strategy, the DFIG output current flowing into the weak grid (simulated by reactor) will produce large voltage drop,

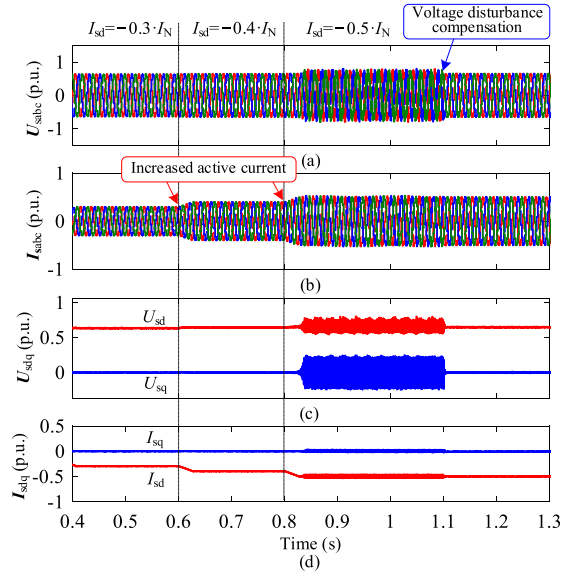

FIGURE 18. Time domain simulation results of DFIG with the proposed control strategy based on voltage disturbance compensation. (a) stator three-phase voltage U_{sabc}; (b) stator three-phase current I_{sabc}; (c) stator dq-axis voltage U_{sdq}; (d) stator dq-axis current I_{sdq}.

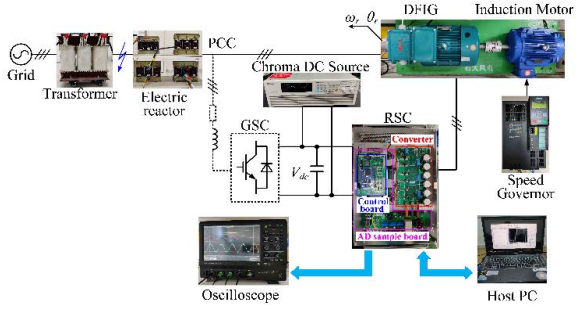

FIGURE 19. Schematic diagram of the experimental platform.

resulting in serious distortion of stator voltage. The distortion is then transmitted to the whole control system through the PLL, resulting in oscillations of the stator current. Under the same operation condition, however, when the proposed control strategy is adopted, the oscillations in the stator voltage and current are greatly suppressed, as shown in Fig. 20(B). From the FFT analysis result of the stator A-phase voltage in Fig. 20, it can be seen that although the enhanced control strategy does not completely eliminate the harmonics in the three-phase waveforms, the magnitude of the main oscillation components get inhibited to a great extent. It proves that the proposed control is capable of improving the stability of DFIG system.

In addition, the dynamic characteristic of the proposed control is also tested, with the results shown in Fig. 21. During the test, at 3s, the active current injected into the weak grid increases from -0.2p.u. to -0.4p.u., and then oscillations occur in the stator voltage and current. However, when the proposed control strategy is triggered at 9s, as shown in Fig. 21, the oscillations in stator voltage and current are suppressed

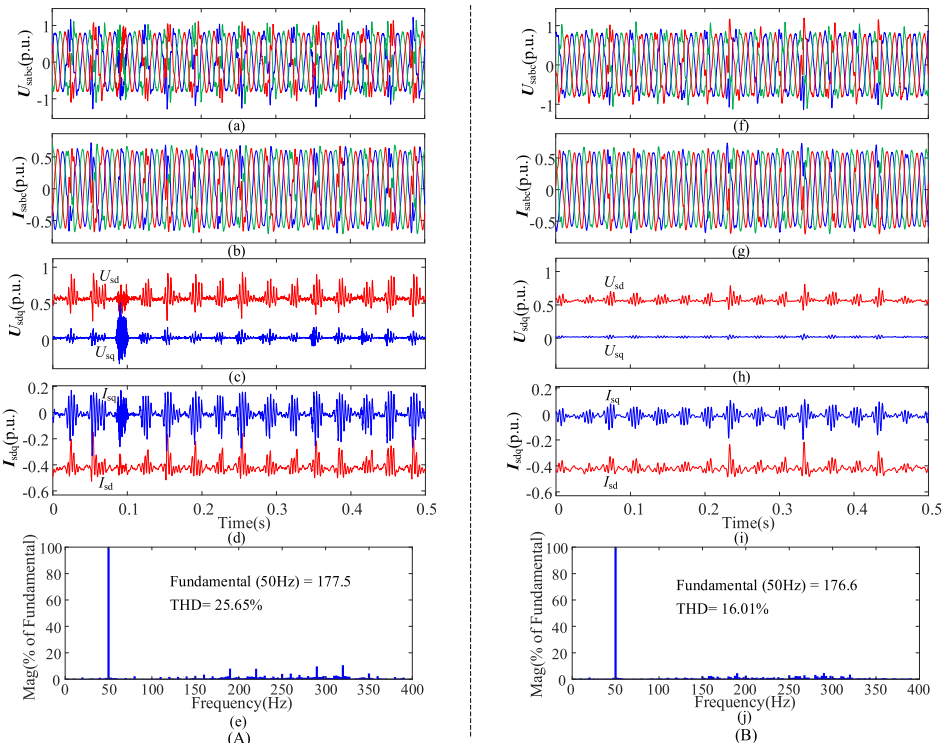

FIGURE 20. Experimental results of DFIG under different control strategies. (A) The traditional control strategy. (B) The proposed optimal control strategy. (a) and (f) stator three-phase voltage U_{sabc}; (b) and (g) stator three-phase current I_{sabc}; (c) and (h) stator dq-axis voltage U_{sdq}; (d) and (i) stator dq-axis current I_{sdq}. (e) and (j) the FFT analysis result of the stator A-phase voltage.

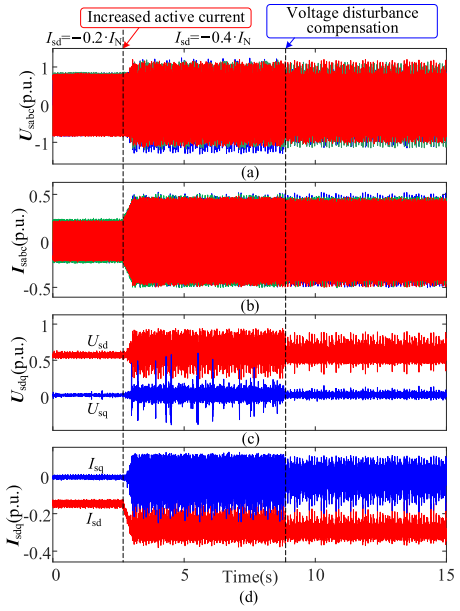

FIGURE 21. Experimental results of DFIG. (a) stator three-phase voltage U_{sabc}; (b) stator three-phase current I_{sabc}; (c) stator dq-axis voltage U_{sdq}; (d) stator dq-axis current I_{sdq}.

significantly, which proves that the proposed control has a satisfactory transient characteristic.

V. CONCLUSION

This paper focuses on the stability mechanism and enhanced control of DFIG-based wind turbines during weak grid conditions. The small-signal admittance model of DFIG-based WTs tied into weak grid is established, which considers the effects of PLL, RCC, and line impedance as well. Then, the impact of the active and reactive currents on the stability of grid-connected system is estimated. Some useful conclusions can be summarized as follows.

1) Injecting active current into weak power grid is not conducive to system stability, while the reactive current has little effect on system stability. In other words, the system stability is mainly determined by the active current.

2) The effect mechanism of the active/reactive current on the system stability reveals that the active current I_{sd} mainly affects the q-axis component of the stator voltage, i.e., U_{sq}, which will be further transmitted into the DFIG control system through the PLL and frame rotating transformation. However, the reactive current I_{sq} primarily influences the d-axis component of the stator voltage, i.e., U_{sd}, in which the disturbance is hard to be transferred further.

3) The proposed enhanced control can extend the stable operation region of the DFIG system. And its steady and transient features during weak AC grid have been proved by the simulations and experiments.

APPENDIX

The proportional and integration coefficients of the PI controllers of PLL and RSC current controller are given in Tab. 3.

TABLE 3. The parameters of PLL and RSC current controller.

K_{p_pll}	50
K_{i_pll}	10
K_{p_rcc}	100
K_{i_rcc}	5400

The key parameters of the second-order high pass filter and compensation coefficient used in the enhanced control strategy are given in Tab. 4.

TABLE 4. The parameters of the enhanced control strategy.

ω_n (rad/s)	628
Q	0.707
K_{com}	0.3

REFERENCES

[1] O. P. Mahela, N. Gupta, M. Khosravy, and N. Patel, "Comprehensive overview of low voltage ride through methods of grid integrated wind generator," *IEEE Access*, vol. 7, pp. 99299–99326, 2019.
[2] P. Sun, J. Yao, R. Liu, J. Pei, H. Zhang, and Y. Liu, "Virtual capacitance control for improving dynamic stability of the DFIG-based wind turbines during a symmetrical fault in a weak AC grid," *IEEE Trans. Ind. Electron.*, vol. 68, no. 1, pp. 333–346, Jan. 2021.
[3] F. Hans, W. Schumacher, and L. Harnefors, "Small-signal modeling of three-phase synchronous reference frame phase-locked loops," *IEEE Trans. Power Electron.*, vol. 33, no. 7, pp. 5556–5560, Jul. 2018.
[4] Y. M. Alsmadi, L. Xu, F. Blaabjerg, A. J. P. Ortega, A. Y. Abdelaziz, A. Wang, and Z. Albataineh, "Detailed investigation and performance improvement of the dynamic behavior of grid-connected DFIG-based wind turbines under LVRT conditions," *IEEE Trans. Ind. Appl.*, vol. 54, no. 5, pp. 4795–4812, Sep./Oct. 2018.
[5] M. Rahimi, "Discussion on 'virtual damping flux-based LVRT control for DFIG-based wind turbine,'" *IEEE Trans. Energy Convers.*, vol. 31, no. 1, p. 407, Mar. 2016.
[6] Z. Xie, Y. Chen, W. Wu, Y. Xu, H. Wang, J. Guo, and A. Luo, "Modeling and control parameters design for grid-connected inverter system considering the effect of PLL and grid impedance," *IEEE Access*, vol. 8, pp. 40474–40484, 2020.
[7] H. Xu, Y. Zhang, Z. Li, R. Zhao, and J. Hu, "Reactive current constraints and coordinated control of DFIG's RSC and GSC during asymmetric grid condition," *IEEE Access*, vol. 8, pp. 184339–184349, 2020.
[8] Y. Song and F. Blaabjerg, "Analysis of middle frequency resonance in DFIG system considering phase-locked loop," *IEEE Trans. Power Electron.*, vol. 33, no. 1, pp. 343–356, Jan. 2018.
[9] M. Zhao, X. Yuan, and J. Hu, "Modeling of DFIG wind turbine based on internal voltage motion equation in power systems phase-amplitude dynamics analysis," *IEEE Trans. Power Syst.*, vol. 33, no. 2, pp. 1484–1495, Mar. 2018.
[10] W. Du, J. Bi, J. Cao, and H. F. Wang, "A method to examine the impact of grid connection of the DFIGs on power system electromechanical oscillation modes," *IEEE Trans. Power Syst.*, vol. 31, no. 5, pp. 3775–3784, Sep. 2016.
[11] R. Liu, J. Yao, X. Wang, P. Sun, J. Pei, and J. Hu, "Dynamic stability analysis and improved LVRT schemes of DFIG-based wind turbines during a symmetrical fault in a weak grid," *IEEE Trans. Power Electron.*, vol. 35, no. 1, pp. 303–318, Jan. 2020.
[12] X. Zou, D. Zhu, J. Hu, S. Zhou, and Y. Kang, "Mechanism analysis of the required rotor current and voltage for DFIG-based wts to ride-through severe symmetrical grid faults," *IEEE Trans. Power Electron.*, vol. 33, no. 9, pp. 7300–7304, Sep. 2018.
[13] S. Ma, H. Geng, L. Liu, G. Yang, and B. C. Pal, "Grid-synchronization stability improvement of large scale wind farm during severe grid fault," *IEEE Trans. Power Syst.*, vol. 31, no. 1, p. 407, Mar. 2016.
[14] J. Kim, E. Muljadi, J.-W. Park, and Y. C. Kang, "Adaptive hierarchical voltage control of a DFIG-based wind power plant for a grid fault," *IEEE Trans. Smart Grid*, vol. 7, no. 6, pp. 2980–2990, Nov. 2016.
[15] X. Zhang, Y. Zhang, R. Fang, and D. Xu, "Impedance modeling and SSR analysis of DFIG using complex vector theory," *IEEE Access*, vol. 7, pp. 155860–155870, 2019.
[16] Y. Xu, H. Nian, T. Wang, L. Chen, and T. Zheng, "Frequency coupling characteristic modeling and stability analysis of doubly fed induction generator," *IEEE Trans. Energy Convers.*, vol. 33, no. 3, pp. 1475–1486, Sep. 2018.
[17] F. Shi, D. Shu, Z. Yan, and Z. Song, "A shifted frequency impedance model of doubly fed induction generator (DFIG)-based wind farms and its applications on S^2SI analysis," *IEEE Trans. Power Electron.*, vol. 36, no. 1, pp. 215–227, Jan. 2021.
[18] A. Adib and B. Mirafzal, "Virtual inductance for stable operation of grid-interactive voltage source inverters," *IEEE Trans. Ind. Electron.*, vol. 66, no. 8, pp. 6002–6011, Aug. 2019.
[19] A. Adib, F. Fateh, and B. Mirafzal, "Smart inverter stability enhancement in weak grids using adaptive virtual-inductance," *IEEE Trans. Ind. Appl.*, vol. 57, no. 1, pp. 814–823, Jan. 2021.

ZHI LI received the B.S. degree from the Shandong University of Science and Technology, Qingdao, China, in 2019. He is currently pursuing the master's degree with the New Energy College, China University of Petroleum (East China). His research interests include modeling and stability analysis of wind power generation systems.

HAILIANG XU (Member, IEEE) received the B.S. degree in electrical engineering from the China University of Petroleum (East China), Qingdao, China, in 2008, and the Ph.D. degree in electrical engineering from Zhejiang University, Hangzhou, China, in 2014.

Since 2018, he has been an Associate Professor with the China University of Petroleum (East China). His current research interests include wind power generation, microgrid, and power quality.

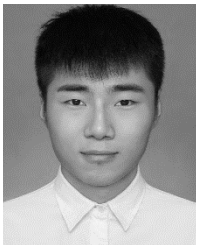

ZHONGXING WANG received the B.S. degree from the China University of Petroleum (East China), Qingdao, China, in 2020, where he is currently pursuing the master's degree with the New Energy College. His research interests include modeling and stability analysis of BDFIG.

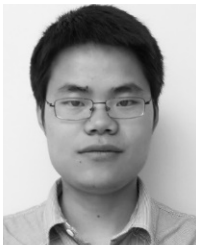

QINGZENG YAN received the B.S. degree in electrical engineering and its automation from the China University of Petroleum (East China), Dongying, China, in 2011, and the Ph.D. degree in electrical engineering from the China University of Mining and Technology, Xuzhou, China, in 2016.

He has been a Lecturer with the College of Information and Control Engineering, China University of Petroleum (East China), since 2017. During 2014 and 2016, he was a Visiting Ph.D. Student with the Electrical Energy Management Group (EEMG), University of Bristol, Bristol, U.K., where he was also a Visiting Scholar, in 2018. His research interests include power electronics, photovoltaic generation systems, advanced topology and control of multilevel converters, and applications of wide-bandgap devices.